

Article

# Transonic Buffet Active Control with Local Smart Skin

Kai Ren <sup>1</sup> , Chuanqiang Gao <sup>1,\*</sup>, Fangqi Zhou <sup>2</sup> and Weiwei Zhang <sup>1</sup>

<sup>1</sup> Department of Fluid Mechanics, School of Aeronautics, Northwestern Polytechnical University, Xi'an 710072, China; renkai@mail.nwpu.edu.cn (K.R.); aeroelastic@nwpu.edu.cn (W.Z.)

<sup>2</sup> High Speed Aerodynamics Research Institute, China Aerodynamics Research and Development Center, Mianyang 621000, China; fqzhou@cardc.cn

\* Correspondence: gaocq@nwpu.edu.cn

**Abstract:** Transonic flight has high economic benefits, but the appearance of transonic buffet limits the flight envelope. The shock control bump currently used for transonic buffet suppression tends to degrade the aerodynamic performance of the non-buffeting state. In this study, a smart skin system is used to eliminate the fluctuating load of transonic buffet by measuring the airfoil lift coefficient as the feedback signal and adjusting the local skin height using data-driven, model-free adaptive control. Since the actuator height is dynamically adjusted only after the occurrence of transonic buffet, the smart skin can completely suppress the fluctuating load and does not affect the aerodynamic performance in the non-buffeting state. The suppression effect of the proposed smart skin on transonic buffet is verified by numerical simulation of the flow. The simulation results show that due to the introduction of closed-loop control, the fluctuating load of transonic buffet can be effectively suppressed for different positions and maximum heights of the actuator. Even when the flow state changes, the robust smart skin system can also achieve the control goal. Therefore, smart skins combining flexible materials and control technologies have the potential to effectively improve the aerodynamic performance of aircraft.

**Keywords:** smart skin; transonic buffet; closed-loop flow control; fluctuating load suppression



**Citation:** Ren, K.; Gao, C.; Zhou, F.; Zhang, W. Transonic Buffet Active Control with Local Smart Skin. *Actuators* **2022**, *11*, 155. <https://doi.org/10.3390/act11060155>

Academic Editors: Ioan Ursu, Hui Tang and Xin Wen

Received: 29 April 2022

Accepted: 8 June 2022

Published: 10 June 2022

**Publisher's Note:** MDPI stays neutral with regard to jurisdictional claims in published maps and institutional affiliations.



**Copyright:** © 2022 by the authors. Licensee MDPI, Basel, Switzerland. This article is an open access article distributed under the terms and conditions of the Creative Commons Attribution (CC BY) license (<https://creativecommons.org/licenses/by/4.0/>).

## 1. Introduction

Transonic flight has high economic benefits, but when the flow state enters above the transonic buffet boundary [1], which consists of Mach number ( $M$ ) and angle of attack ( $\alpha$ ), transonic buffet flow [2] occurs on the wing surface. This is a kind of flow instability phenomenon caused by shock wave/boundary layer interaction, which is manifested as a large oscillation of shock wave on the wing surface, causing fluctuation of lift, affecting flight comfort and safety, easily causing fatigue damage to the wing structure, and limiting the flight envelope in the transonic section. In order to eliminate the fluctuating load of transonic buffet and improve the flow stability, various passive and active control schemes are used to modify the flow in the shock wave/boundary layer interaction region and trailing edge region [3]. The control devices mainly include vortex generator [4,5], shock control bump [6,7], streamwise slot [8], plasma actuator [9,10], and trailing edge flap [11,12]. Unfortunately, due to the complexity of shock buffet, a robust control scheme for eliminating shock buffet load has not been obtained in experiments. Researchers seek to analyze the advantages and disadvantages of different control schemes through numerical simulation, so as to provide some support for the realization of shock buffet control. The active control with the trailing edge flap as the actuator can effectively eliminate the fluctuating load, but it will occupy the control channel of the flap surface. Passive control represented by shock control bump (SCB) is widely studied because of its simple structure and effective improvement of transonic buffet boundary. However, the problem of SCB is that when the position and shape of the SCB are determined, it can only eliminate the buffeting load in the partial incoming flow state, and will reduce the aerodynamic performance in

the non-buffeting state. Therefore, the smart skin technology of a deformable wing [13] can combine the advantages of both control schemes mentioned above. The shape of the bump can be dynamically adjusted after transonic buffet occurs, which has the potential to effectively eliminate the transonic buffeting load without affecting the aerodynamic performance of the non-buffeting state.

With the development of new intelligent materials and distributed sensing and control technology, the deformable wing technology is evolving towards the direction of intelligence and flexibility. The use of intelligent materials such as piezoelectric materials [14] and shape memory alloys [15] to drive the deformation of aircraft and achieve the integration of flexible skin materials, structure, and actuator is a current research hotspot and a development direction for future applications. Table 1 compares the actuation performance of two intelligent materials: piezoelectric materials and shape memory alloys. Among the advantages of the piezoelectric materials is the fast response speed, while the shape memory alloy has the advantage of large output force and output displacement, compared to conventional wings that improve the aerodynamic performance of an aircraft under only a few specific flight conditions through the simple rigid deformation of flaps, leading edge slats, and other mechanisms. The intelligent deformable wings composed of intelligent deformable materials combined with distributed sensors and microcontrollers do not produce discontinuous changes and abrupt curvature changes, or reduce the separation of flow, and can optimize deformation parameters for each flight condition, which has better flight performance [16,17]. The deformable wing includes folding wing [18], flexible trailing edge [19], adaptive wingtip [20], active camber wing [21] and smart skin [22]. To enhance the performance of the aircraft, researchers use wings with variable camber [23,24], variable thickness [25], variable trailing edge deflection [19,26], and deformable winglets [27] to improve aerodynamic performance; use adaptive wings with adjustable maximum height and maximum height position to improve stall aerodynamic performance [28]; use deformable wings to adapt to different flight environments [29]; use flexible trailing edges to reduce structural weight of swept-wing aircraft [30]; use deformable trailing edges to control the boundary layer flow to reduce noise [31]; use adaptive wingtips to reduce fuel consumption and gust loads through cant, twist, and camber deformation [20]; use smart skin to adjust the inlet shape to make the engine have good performance over a wide range of rotation speed range [32]; and use smart skin to suppress panel flutter [33] and wing flutter [34].

**Table 1.** Comparison of intelligent material actuation performance.

Intelligent Material	Response Speed	Output Force	Output Displacement	Frequency Band
Piezoelectric materials	fast	moderate	small	wide
Shape memory alloys	slow	high	large	narrow

In this study, smart skin technology is used to suppress the fluctuating load of transonic buffeting flow. Smart skin technology forms the neural network of aircraft by implanting intelligent structures within the aircraft skin and other components, including detection elements (sensors), microprocessor control systems (signal processors), drive elements (micro actuator), and interconnecting lines, etc. It can not only sense its own physical conditions (such as structural damage), but also be sensitive to the external environment (such as incoming flow condition). In this way, the components and even the whole aircraft body are endowed with self-monitoring, self-correction, self-adaptation, and memory, thinking, judgment, and response functions.

This paper is organized as follows: In Section 2, the composition of the smart skin system and the flow numerical simulation method to simulate the control performance are introduced. In Section 3, the adopted control method is introduced and simulations are performed to verify the effectiveness of the method in suppressing the transonic buffet fluctuating load. Section 4 analyzes the influence of smart skin system parameters on

the control effect and tests the robustness of the system to different incoming flow states. Conclusion and discussion are presented in Section 5.

## 2. Smart Skin System and Simulation Method

### 2.1. Smart Skin System

The smart skin system includes sensors, microprocessor control systems, micro actuators, and interconnecting lines. The feedback signal used for the active control of transonic buffet is mainly the force coefficient and the wall pressure. Compared with the wall pressure, the lift coefficient ( $C_l$ ) is obtained by the integration of the pressure distribution ( $C_p$ ), which is smooth and beneficial to the stability of the system. Therefore, the lift coefficient is used as a feedback signal in the smart skin system. Since there is a direct proportional relationship between the lift force and the wing root bending moment, the lift coefficient is obtained by measuring the wing root bending moment using strain gauges. The design of the control law is described in Section 3.1.

The micro actuator uses the local deformation skin with adjustable height; the shape of deformation skin is a widely used Hicks–Henne shape function [7], as shown in Figure 1. The shape parameters include: (1) the length of deformation skin,  $l_b$ , (2) the starting position of deformation skin,  $x_0$ , (3) crest location,  $x_{hmax}/l_b$ , and (4) the height of deformation skin,  $h_b$  (defined as the ratio of the actual height to the chord length). The height of deformation skin is output by the control law and can be adjusted dynamically. The Hicks–Henne shape function is

$$\begin{aligned} f_b(x_b) &= h_b H(x_b) \\ H(x_b) &= \sin^4(\pi x_b^m), \quad m = \ln(0.5) / \ln(x_{hmax}/l_b) \end{aligned} \tag{1}$$

where,  $x_b$  is the dimensionless chordwise position of deformation skin, which is defined as  $0 \leq x_b = (x - x_0)/l_b \leq 1$ . In this study, the length of deformation skin is taken to be 0.2 times the chord length,  $l_b = 0.2 c$ , and the shape of deformation skin is symmetric, and the crest location is  $x_{hmax}/l_b = 0.5$ .

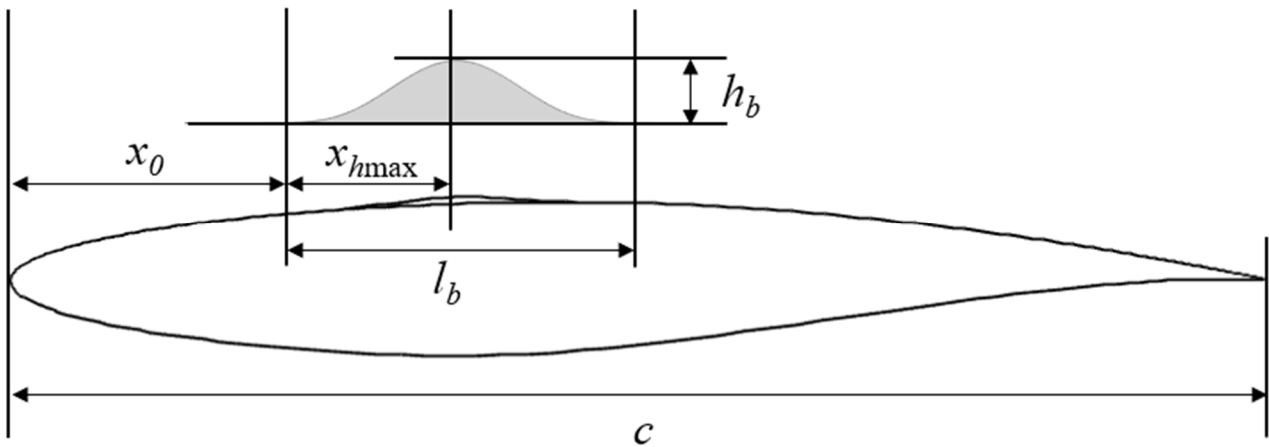


Figure 1. Diagram of smart skin micro actuator.

### 2.2. Flow Numerical Simulation Method

In this study, the control performance of the smart skin system is analyzed by flow numerical simulation, and the numerical simulation uses the unsteady Reynolds-averaged Navier–Stokes (URANS) solver based on the finite volume method. The two-dimensional compressible URANS governing equations can be expressed as:

$$\frac{\partial}{\partial t} \iiint_{\Omega} W dV + \iint_{\partial\Omega} F^i(W, V_{grid}) \cdot n dS = \iint_{\partial\Omega} F^v(W) \cdot n dS \tag{2}$$

where  $W$  is the flux variables,  $F^i(W, V_{grid})$  is the inviscid flux,  $F^v(W)$  is the viscous flux,  $V_{grid}$  is the grid velocity,  $\Omega$  is the control volume,  $\partial\Omega$  is the control volume boundary, and  $n$  is the unit vector of normal direction outside the boundary.

The S-A turbulence model is introduced to close the Reynolds-averaged equation, and the spatial discretization and time integration of turbulent and mean flows are carried out in a loosely coupled way. The second-order advection upstream splitting method (AUSM) scheme is used to evaluate the inviscid flux with a reconstruction technique. The viscous flux term is discretized by the standard central scheme. In the turbulence model, the convective term is discretized by the second-order AUSM scheme and the destruction term by the second-order central scheme. For unsteady computations, the dual time stepping method is used to solve the governing equations. At the sub-iteration, the fourth-stage Runge–Kutta scheme is used with a local time stepping.

Due to the airfoil shape change during the numerical simulation, a grid deformation method is required to ensure the update and deformation of the airfoil surface and the solution domain grid. The grid deformation scheme uses the radial basis function (RBF) interpolation method [35].

The controlled object adopts the transonic buffet of RAE2822 airfoil, and the computational flow domain is discretized by a hybrid unstructured grid. The far field extends 20 chords away from the airfoil. There are 12,958 surface nodes and 40 layers of structured viscous grids around the airfoil. The distance between the first layer and the wall in the perpendicular direction is  $5 \times 10^{-6}$  chords ( $y^+ < 1$ ). For a transonic flow:  $M = 0.73$ ,  $\alpha = 3.19^\circ$ , and  $Re = 6.5 \times 10^6$ . Figure 2 shows the comparison between the calculated pressure distribution and the experimental result [36], which is basically consistent with each other. By fixing the Mach number of the incoming flow and simulating different angles of attack (the interval of angles of attack is  $0.1^\circ$ ) it can be determined whether the transonic buffet occurs. The buffet onset boundary obtained is shown in Figure 3, which is almost consistent with the onset boundary [7] calculated by Tian et al.

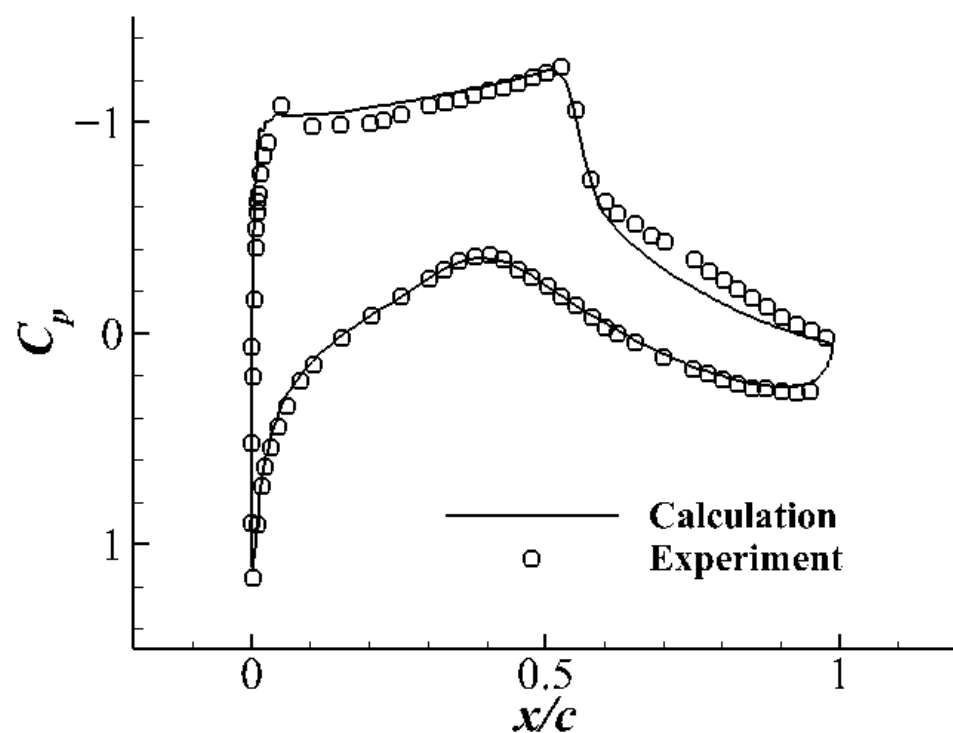
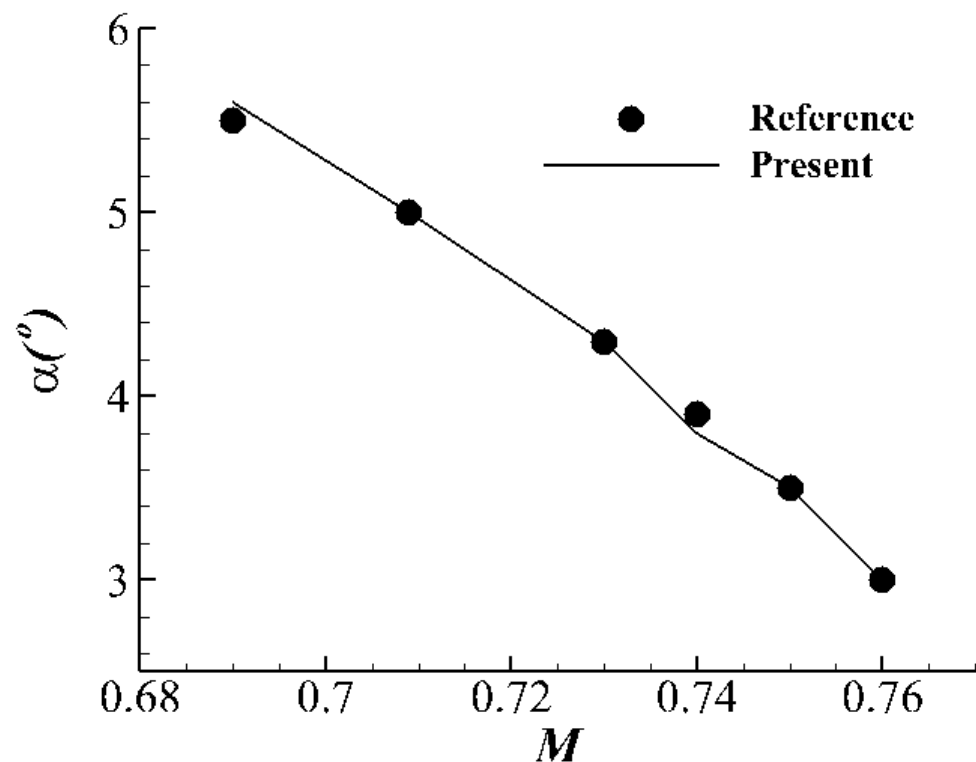


Figure 2. Comparison of pressure distribution on airfoil surface.



**Figure 3.** Comparison of transonic buffet onset boundary.

Choose the incoming flow state:  $M = 0.75$ ,  $\alpha = 4^\circ$ , and  $Re = 6.5 \times 10^6$  to simulate the time history of buffet. It can be seen from Figure 3 that this flow state is above the buffet onset boundary, and when the control is not turned on, the system will have a large lift fluctuation, as shown in Figure 4. Figure 5 shows the flow field pressure contours at different moments, corresponding to the four moments in Figure 4 ( $a$  and  $c$  are the middle positions when the shock wave moves upstream and downstream, respectively, and  $b$  and  $d$  are the most upstream and downstream positions of the shock wave, respectively). When the shock wave moves upstream, the length of the trailing edge separation bubble increases, and when the shock wave moves downstream, the separation bubble at the foot of the shock wave and the trailing edge separation bubble approach and merge gradually. From the pressure contours, it can be seen that the dimensionless chordwise range of the shock wave oscillation for this flow condition is 0.45~0.56, and the shock wave is at the most downstream position when the lift coefficient is maximum, and vice versa.

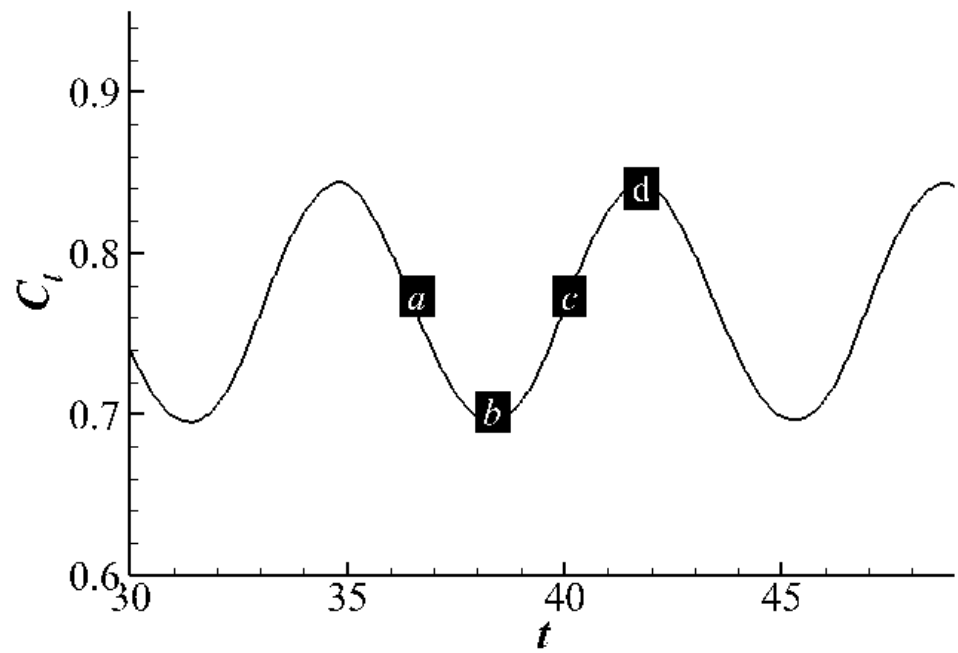


Figure 4. Lift coefficient time history.

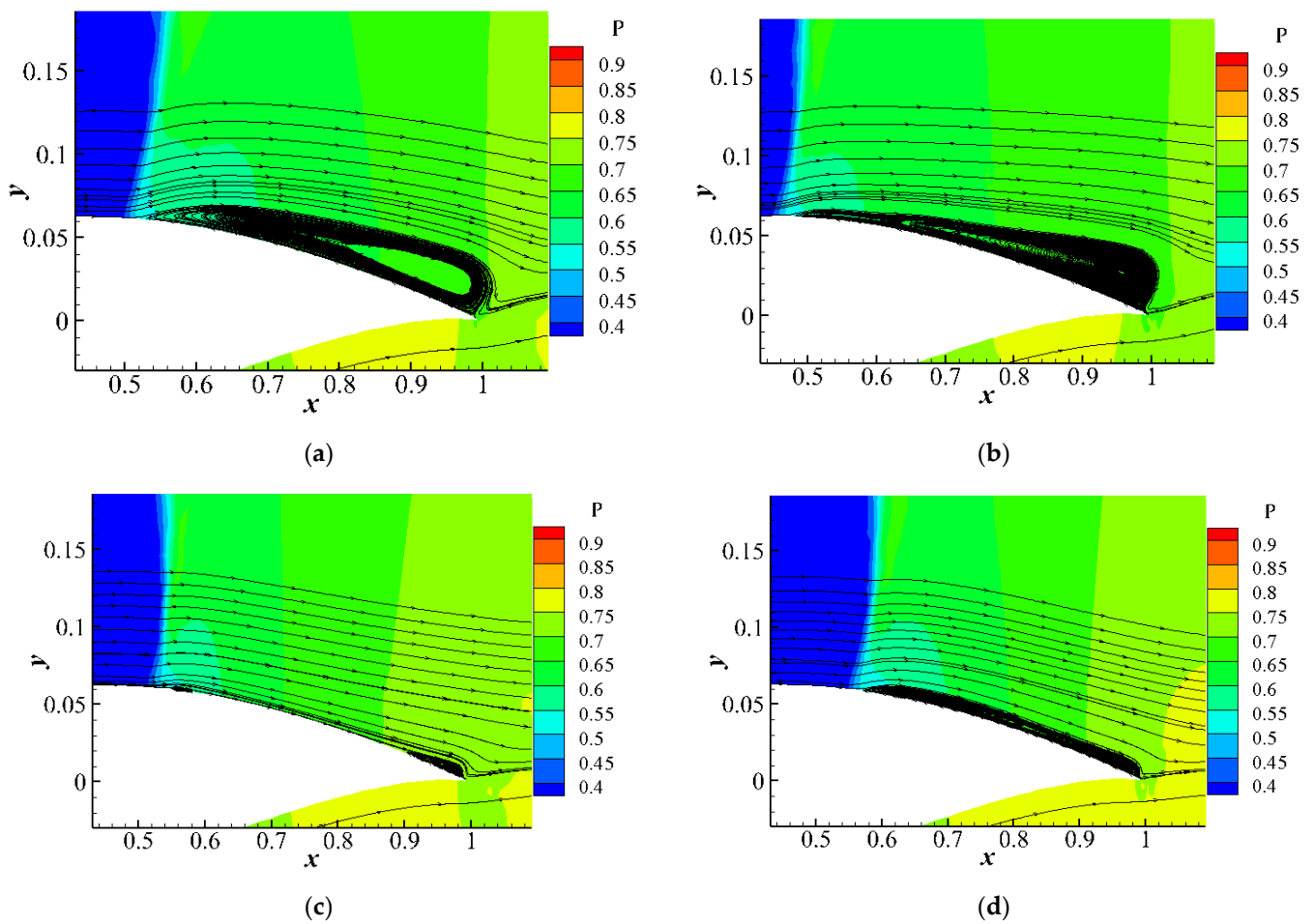


Figure 5. Local pressure contours and streamlines of flow field at different moments: (a) moment *a*; (b) moment *b*; (c) moment *c*; (d) moment *d*.

### 3. Transonic Buffet Control

#### 3.1. Model-Free Adaptive Control

Model-free adaptive control [37] is a data-driven control method. Its basic idea is to equivalently transform the discrete-time nonlinear system into a dynamic linearized data model based on the input and output data of the system at each moment using a pseudo partial derivative (PPD). Without establishing an accurate mathematical model of the flow system, the data-driven adaptive control of the flow system is achieved by estimating the system PPD online using the input and output data of the flow system, and then minimizing a given cost function.

For the transonic buffet flow system in this study, the feedback signal is the lift coefficient,  $C_l$ , the control signal is the actuator height,  $h_b$ , and the controlled plant can be described by the following single-input, single-output, discrete-time nonlinear system:

$$C_l(k+1) = f(C_l(k), \dots, C_l(k-n_o), h_b(k), \dots, h_b(k-n_i)) \quad (3)$$

where  $n_i$  and  $n_o$  are unknown input and output delay orders, respectively, and  $f(\cdot)$  is an unknown nonlinear function describing the relationship between lift coefficient and actuator height.

Based on PPD, the above flow plant is equivalently transformed into the following dynamic linearized data model:

$$C_l(k+1) = C_l(k) + \phi(k)\Delta h_b(k) \quad (4)$$

where  $\phi(k)$  is the PPD of system (3), it is estimated from the historical input and output data of the system by minimizing the following cost function:

$$J(\phi(k)) = |C_l(k) - C_l(k-1) - \phi(k)\Delta h_b(k-1)|_2 + \mu|\phi(k) - \hat{\phi}(k-1)|^2 \quad (5)$$

The estimation algorithm of the PPD (where  $\mu > 0$  is the weighting factor):

$$\hat{\phi}(k) = \hat{\phi}(k-1) + \frac{\eta\Delta h_b(k-1)}{\mu + \Delta h_b(k-1)^2} (\Delta C_l(k) - \hat{\phi}(k-1)\Delta h_b(k-1)) \quad (6)$$

$\eta \in (0, 1]$  is the update step of PPD, which can make the algorithm more flexible, and  $\eta = 1$  is taken in all of this paper.

In order to eliminate fluctuating load of the transonic buffet flow and improve the flow stability, the following cost function are considered:

$$J(h_b(k)) = |C_l^*(k+1) - C_l(k+1)|_2 + \lambda_1|h_b(k) - h_b(k-1)|_2 + \lambda_2|h_b(k) - h_{b0}|^2 \quad (7)$$

where  $C_l^*(k+1)$  is the desired lift coefficient,  $h_{b0}$  is the initial height of the actuator, and  $\lambda_1$  and  $\lambda_2$  are positive weighting factors. The first term of the cost function is used to limit the deviation between the lift coefficient and the desired lift coefficient, and the second term is used to limit the change of the actuator height. When the unstable steady flow of transonic buffet cannot be obtained in advance, the corresponding desired lift coefficient cannot be obtained, so the desired lift coefficient is taken as the time-averaged lift coefficient, and the deviation between the actuator height and the initial height of the actuator is limited by introducing the third term of the cost function.

Combined with the dynamic linearized data model (4) to minimize the cost function (7), the control law is:

$$h_b(k) = \frac{1}{\lambda_1 + \lambda_2 + \phi(k)^2} \left( \phi(k)(C_l^*(k+1) - C_l(k)) + (\lambda_1 + \phi(k)^2)h_b(k-1) + \lambda_2 h_{b0} \right) \quad (8)$$

The control system block diagram is shown in Figure 6. The loop in the upper part of the block diagram is an adaptive loop, indicating that the adaptive law uses the input and

output data of the system to estimate the PPD online and adjust the controller parameters when the plant parameters change, so as to make the system work in an optimal or near-optimal state. The loop of the lower part is a general feedback loop, which is obtained by minimizing the cost function.

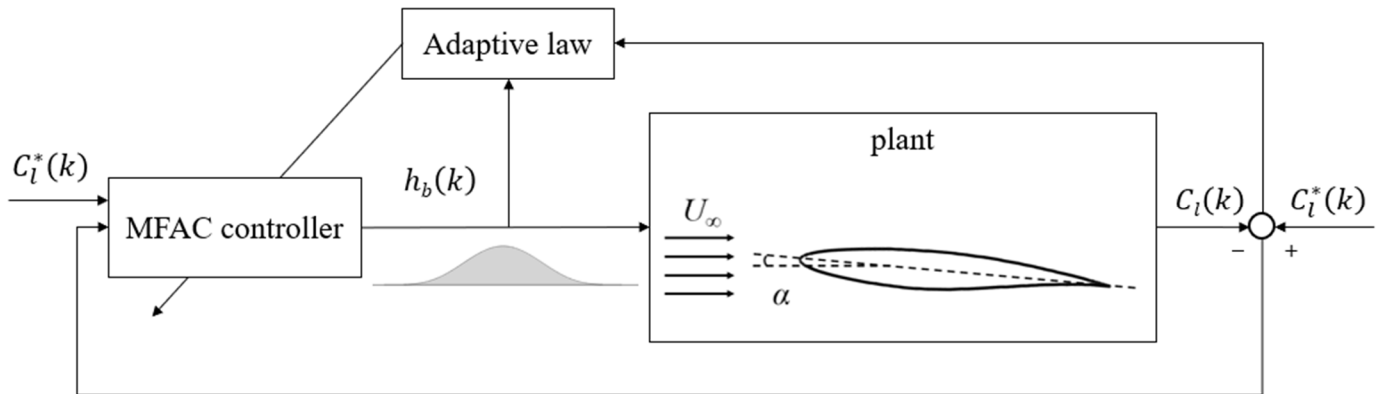


Figure 6. Block diagram of model-free adaptive control system.

### 3.2. Numerical Simulation and Mechanism Analysis of Control Law

For the incoming flow state of  $M = 0.75$ ,  $\alpha = 4^\circ$ , and  $Re = 6.5 \times 10^6$ , it can be seen from Section 2.2 that this state is above the buffet onset boundary. When the control is not turned on, the dimensionless chordwise range of the shock wave oscillation is 0.45–0.56. Smart skin system is used to eliminate the fluctuating load in this state. According to the analysis results by Tian et al., the fluctuating load can be effectively suppressed when the bump is located after the shock wave [7], so the range of actuator is chosen to be 0.55–0.75, that is, the starting position of deformation skin  $x_0 = 0.55$ , and the length of deformation skin  $l_b$  is  $0.2 c$ .

The transonic buffet fluctuating load in this state is suppressed by the above control system configuration. The time history of control signal (actuator height,  $h_b$ ), feedback signal (lift coefficient,  $C_l$ ), and drag coefficient ( $C_d$ ) are shown in Figure 7. It can be seen that when the control is turned on, the fluctuating load ( $C_l$  and  $C_d$ ) has been completely eliminated after a few buffeting cycles, and the actuator height has returned to the initial 0, that is, the airfoil returns to the shape of RAE2822 airfoil. The maximum height of actuator during the control process is 0.00299; there is no additional increase in airfoil drag, and the final steady flow field pressure contour is shown in Figure 8.

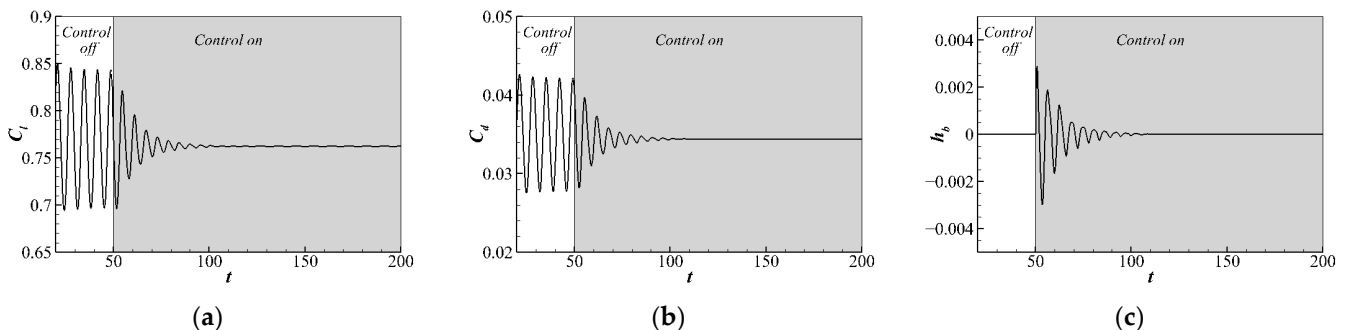


Figure 7. Time history of the system: (a) lift coefficient; (b) drag coefficient; (c) actuator height.

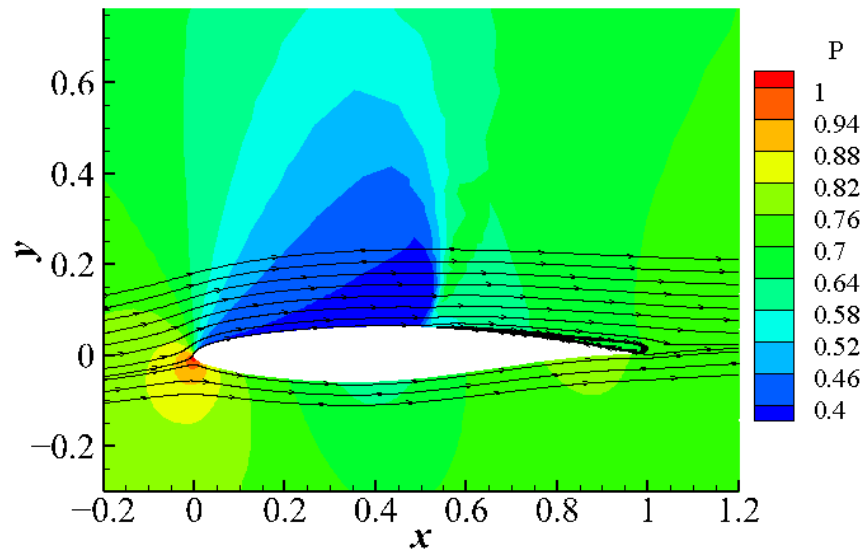


Figure 8. Flow field pressure contour and streamlines after control convergence.

Figure 9 shows the time history of the shock wave dimensionless position  $x_{sw}/c$  and the height of the actuator. It can be seen that the height of the actuator located at the downstream of the shock wave is close to the lowest when the shock wave is at the most downstream, and the height of the actuator is close to the highest when the shock wave is at the most upstream. By changing the height of the actuator, the oscillation of the shock wave is limited, thus eliminating the fluctuating load of the buffet. Figure 10 shows the pressure contour and streamlines for the four moments in Figure 9;  $b'$  and  $d'$  are the middle positions where the shock wave moves downstream and upstream, respectively, and  $a'$  and  $c'$  are the most upstream and downstream positions of the shock wave, respectively. When the shock wave moves from upstream to downstream, the height of the actuator decreases, which limits the movement of the separation bubble at the shock wave foot to downstream and prevents the merging of the separation bubble at the shock wave foot with the trailing edge separation bubble. When the shock wave moves upstream, the actuator height increases, which limits the growth of the trailing edge separation bubble upstream.

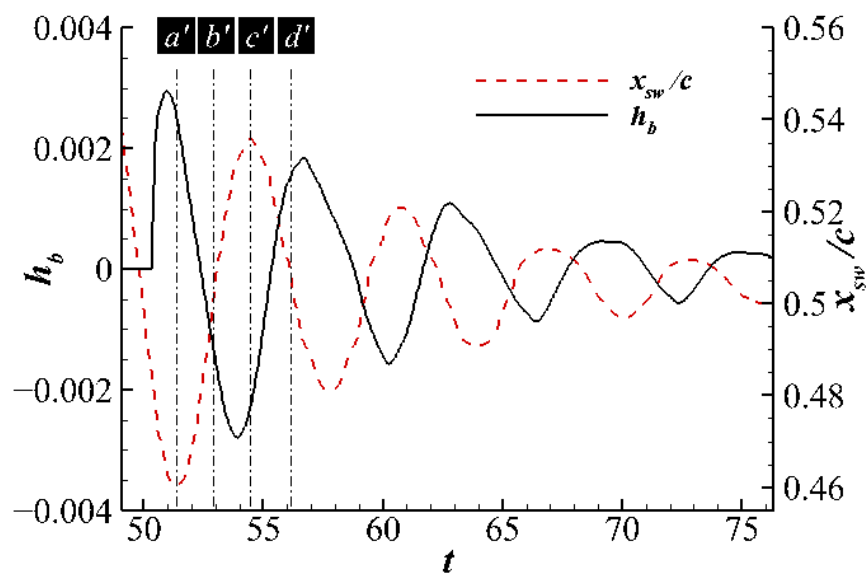
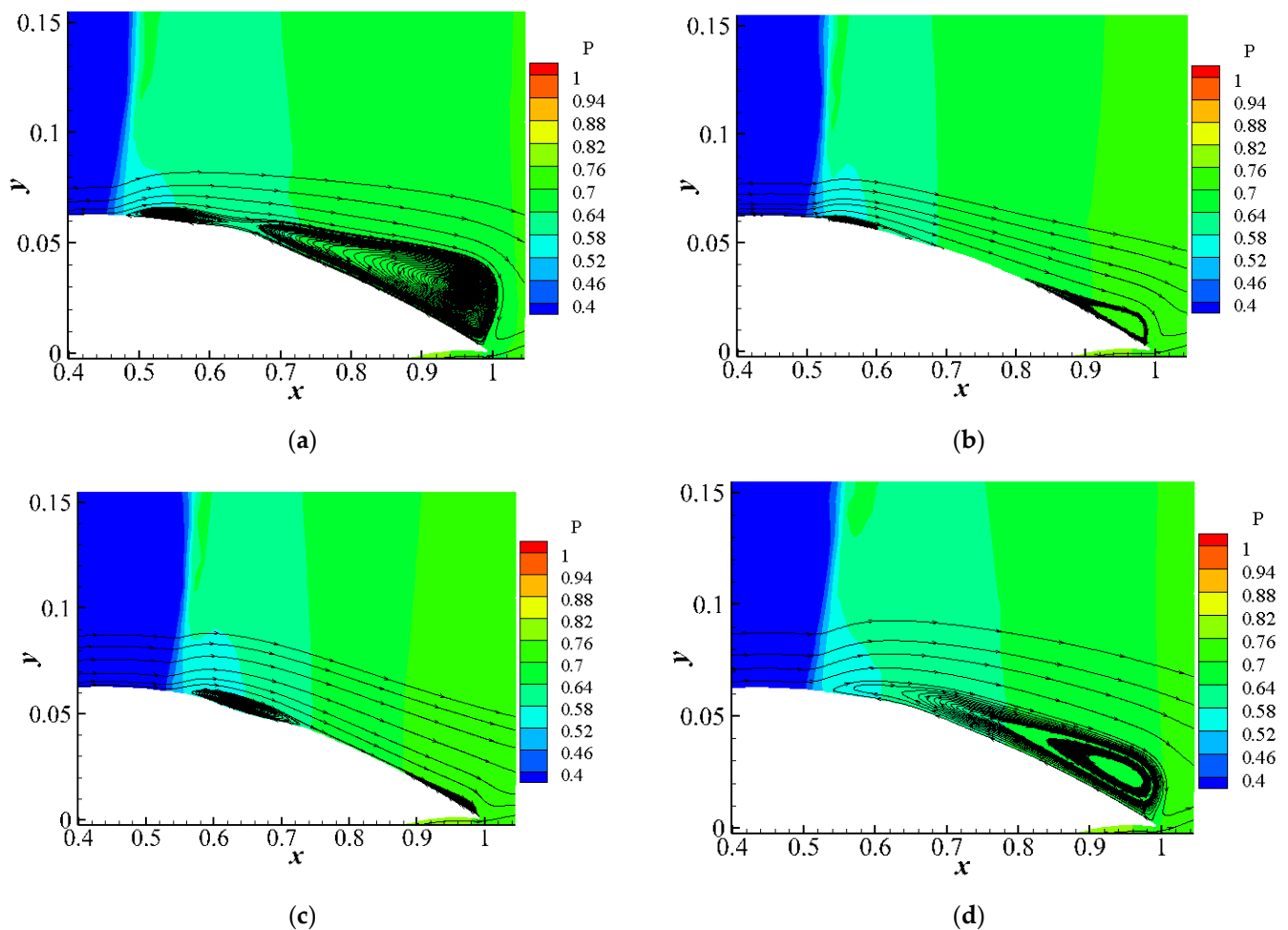


Figure 9. Time history of the shock wave position and the height of the actuator.



**Figure 10.** Local pressure contours and streamlines of flow field at different moments: (a) moment  $a'$ ; (b) moment  $b'$ ; (c) moment  $c'$ ; (d) moment  $d'$ .

#### 4. Smart Skin Performance Analysis

##### 4.1. The Influence of Actuator Position

In the previous section, for the incoming flow state of  $M = 0.75$ ,  $\alpha = 4^\circ$ , and  $Re = 6.5 \times 10^6$ , the dimensionless chordwise range of the shock wave oscillation is 0.45~0.56, and the actuator range is chosen to be 0.55~0.75. In this section, the influence of actuator position on the buffeting load suppression is analyzed. Two actuator positions are selected: (1) the actuator position is upstream of the shock wave oscillation range (actuator range: 0.25~0.45); (2) the actuator position coincides with the shock wave oscillation range (actuator range: 0.4~0.6). The input and output time history of control system are shown in Figures 11 and 12, respectively. It should be noted that in Section 3.2, we analyzed that for the actuator located downstream of the shock wave, when the shock wave was at the most downstream, the height of the actuator was close to the highest. For the actuator located upstream of the shock wave (actuator range: 0.25~0.45), the height of the actuator should be close to the lowest when the shock wave is at the most downstream. That is, the initial value of the PPD in the control law should be opposite to the sign in Section 3.2.

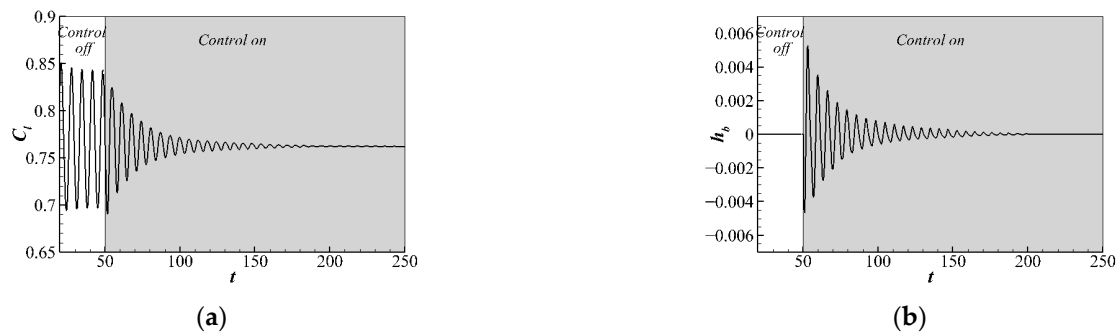


Figure 11. Time history of the system (actuator range: 0.25–0.45): (a) lift coefficient; (b) actuator height.

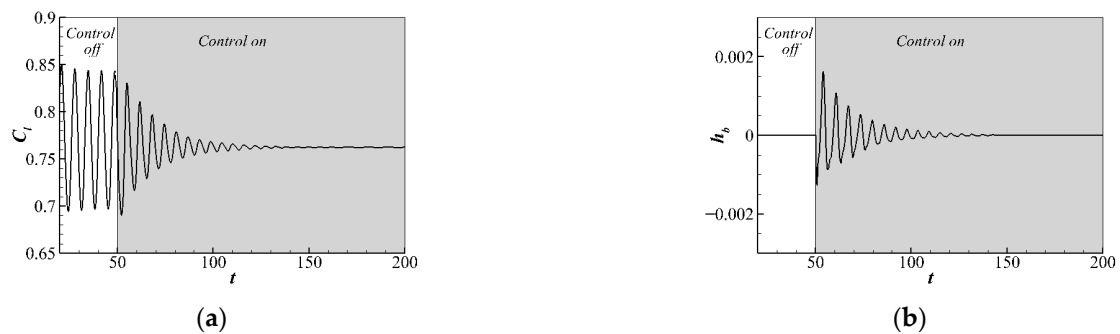


Figure 12. Time history of the system (actuator range: 0.4–0.6): (a) lift coefficient; (b) actuator height.

From Figures 11 and 12, we find that the required actuator height is smaller when the actuator position is close to the oscillation range of shock wave. As shown in Figure 13, we compare the maximum height of the actuator for different crest chordwise positions under the premise of basically the same settling time. Because the function of the actuator is to suppress the oscillation of the shock wave and to prevent the merging of the separation bubble at the shock wave foot and the trailing edge separation bubble, the position of the actuator far away from the shock wave needs a larger height to prevent the merging of the two separation bubbles, and to generate enough pressure disturbance to suppress the oscillation of the shock wave.

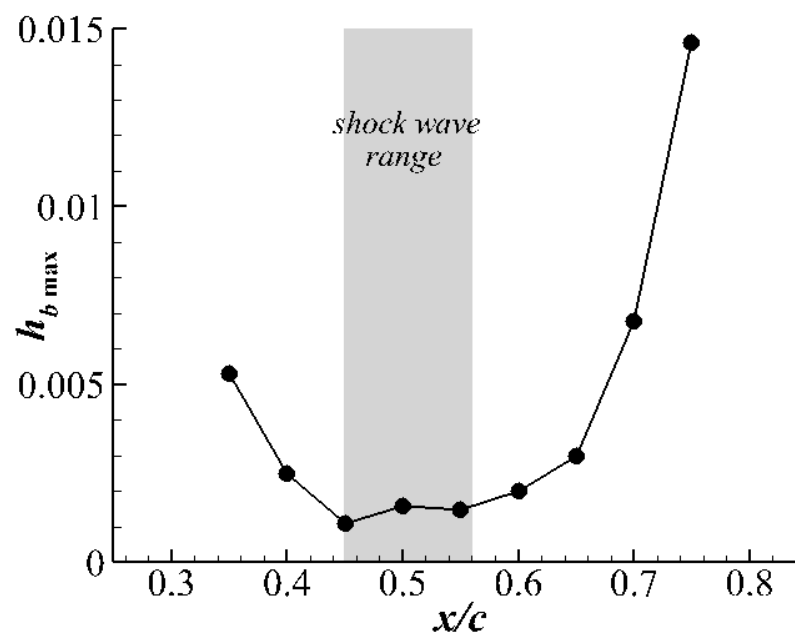
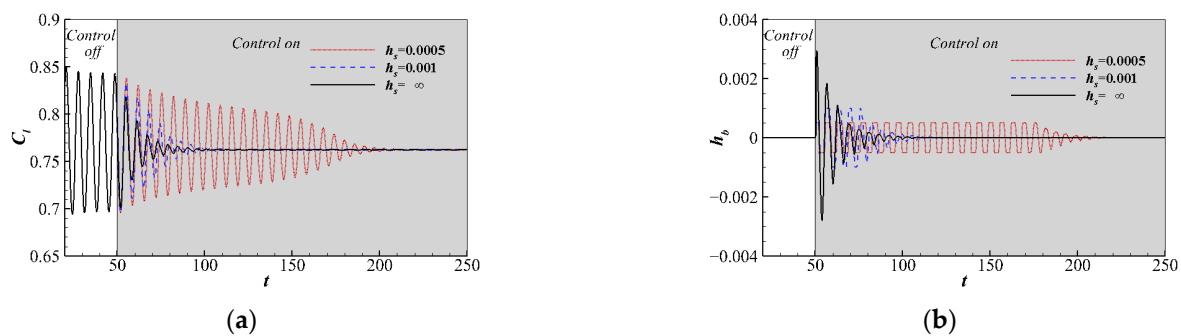


Figure 13. Relationship between maximum height of actuator and crest chordwise position.

#### 4.2. The Influence of Actuator Height

Real wings design often has multiple constraints, such as the wing volume will limit the amplitude of the actuator subsidence, and actuator structure and drag constraints will limit the maximum height of the actuator. Therefore, this subsection will analyze the performance change of the smart skin when the actuator height has the maximum amplitude limit  $h_s$  for the incoming flow state of  $M = 0.75$ ,  $\alpha = 4^\circ$ , and  $Re = 6.5 \times 10^6$ , and the actuator range of 0.55~0.75. As can be seen in Figure 14, the smart skin system can eliminate the transonic buffet fluctuating load under different restrictions of maximum height of the actuator, but with the decrease of the maximum actuator height, the system settling time gradually increases. According to the previous smart skin control mechanism, the phase relationship between the actuator height and the shock wave position (or lift coefficient) plays a decisive role, while the height only affects the dynamic characteristics such as the settling time.



**Figure 14.** Influence of actuator height constraint  $h_s$  on dynamic characteristics of the control system: (a) time history of lift coefficient; (b) time history of actuator height.

As shown in Table 2, the required actuator height for active control can be smaller than that for a passive bump device located immediately downstream of the shock wave, which reduces the requirement for the actuator and is conducive to engineering implementation. Although compared with passive control, active control requires energy input from the time history of input and output of the control system; the output displacement of actuator and settling time are small, so the energy input required is acceptable.

**Table 2.** Maximum height of actuator required for different control strategy.

Control Strategy	Passive Control		Active Control
	Jones et al. [6]	Tian et al. [7]	Present
entry 2	0.012	0.008	less than 0.003

#### 4.3. Robustness of The Control Law

Due to the existence of atmospheric turbulence, the incoming flow state may change, and the dynamics characteristics of the transonic buffet flow system will change, which is manifested in the change of the oscillation range of shock wave, the mean value, and fluctuation amplitude of lift, such as for the other two states above the buffet onset boundary: (1)  $M = 0.73$ ,  $\alpha = 4.8^\circ$ , and  $Re = 6.5 \times 10^6$ , and (2)  $M = 0.71$ ,  $\alpha = 5.5^\circ$ , and  $Re = 6.5 \times 10^6$ . In state (1), oscillation range of shock wave is from 0.35~0.55, and fluctuation range of lift coefficient is 0.723~0.994. In state (2), oscillation range of shock wave is from 0.24~0.48, and fluctuation range of lift coefficient is 0.673~1.042. Figures 15 and 16 show the lift coefficient, drag coefficient, and actuator height time history of the system using smart skin to suppress the fluctuating load in the above two incoming flow states, respectively, and the actuator range from 0.55 to 0.75. It can be seen from the Figures 15 and 16 that the control strategy in this study has strong robustness, and after turning on the control, by adjusting the height

of smart skin, the large fluctuating load of transonic buffet can be completely eliminated, and there is no additional increase in airfoil drag. Compared with state (1), the angle of attack of state (2) increases, the shock wave position moves forward, and the fluctuating amplitude of lift coefficient increases, so the maximum height required to suppress the fluctuating load in state (2) increases.

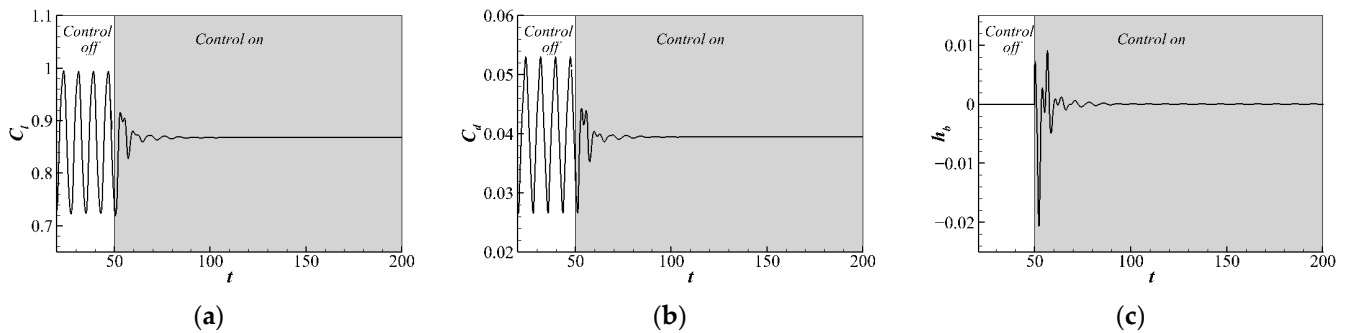


**Figure 15.** Time history of the system ( $M = 0.73$ ,  $\alpha = 4.8^\circ$ ): (a) lift coefficient; (b) drag coefficient; (c) actuator height.

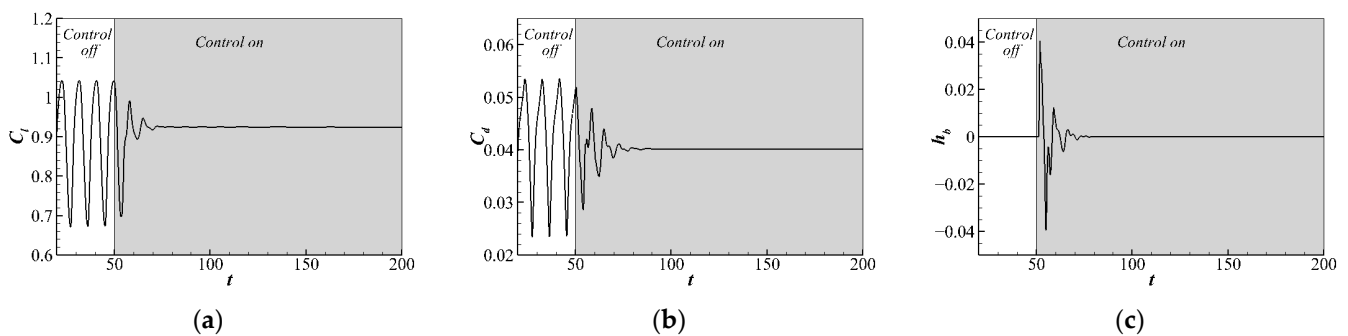


**Figure 16.** Time history of the system ( $M = 0.71$ ,  $\alpha = 5.5^\circ$ ): (a) lift coefficient; (b) drag coefficient; (c) actuator height.

## 5. Conclusions

In this study, the smart skin system is used to suppress the fluctuating load of transonic buffet flow for RAE2822 airfoil. The smart skin system uses the lift coefficient as feedback signal and adopts a model-free adaptive control to dynamically adjust the local skin height of airfoil. When the incoming flow state enters above the transonic buffet onset boundary, by preventing the merging of the separation bubble at the shock wave foot with the trailing edge separation bubble, the smart skin system can completely suppress the fluctuating load and does not affect the aerodynamic performance in the non-buffeting state. From the time history of the control system input and output, the system has a short settling time and does not need too large an output displacement, so the piezoelectric material with high precision of displacement control, fast response speed, low power consumption, and small size can be used as the actuator.

By analyzing the control performance of the smart skin system, the following conclusions were obtained:

- (1) The smart skin system can completely suppress the fluctuating load regardless of whether the actuator position is upstream or downstream of the shock wave, but the maximum height of the actuator required increases when the actuator position is far away from the shock wave oscillation range.
- (2) The fluctuating load of transonic buffet can be completely suppressed under different maximum height constraints, and the height constraint will affect the dynamic performance of the system, such as settling time.

- (3) When the incoming flow state changes, although the oscillation range of shock wave and the fluctuation range of lift coefficient change greatly, the buffeting load in different incoming flow states can be suppressed by the model-free adaptive control with the mean value of the lift coefficient as the desired output of the control system.

The above research is carried out in a simulation environment in order to provide some theoretical support for the realization of shock buffeting control. To realize the control of shock buffet, more detailed parameters, such as the specification and distribution of sensors and the bandwidth and hysteresis of actuators, need to be further studied.

With the progress of material and control technology, new flexible controllers such as smart skin can have more flexible control methods without abrupt curvature changes on the surface of the aircraft, and have the ability to obtain the best control effect through adaptive and intelligent control for different flight conditions, which can greatly improve the aerodynamic performance of the aircraft.

**Author Contributions:** K.R. designed the controller and writing-original draft preparation.; C.G. conceived the original ideals, review; F.Z. proposed the comment for the paper; W.Z. provided research methods, supervision. All authors have read and agreed to the published version of the manuscript.

**Funding:** This research was funded by the National Natural Science Foundation of China (No. 11902269), the Aviation Science Foundation of China (No. 2019ZH053003), the Fundamental Research Funds for the Central Universities, and State Key Laboratory of Aerodynamics innovation Fund Project (JBKYC190102).

**Data Availability Statement:** Not applicable.

**Acknowledgments:** Fangqi Zhou is particularly grateful for the support of the State Key Laboratory of Aerodynamics innovation Fund Project.

**Conflicts of Interest:** The authors declare no conflict of interest.

## References

- Gao, C.; Zhang, W.; Kou, J.; Liu, Y.; Ye, Z. Active control of transonic buffet flow. *J. Fluid Mech.* **2017**, *824*, 312–351. [[CrossRef](#)]
- Giannelis, N.F.; Vio, G.A.; Levinski, O. A review of recent developments in the understanding of transonic shock buffet. *Prog. Aerosp. Sci.* **2017**, *92*, 39–84. [[CrossRef](#)]
- Gao, C.; Zhang, W.; Ye, Z. Numerical study on closed-loop control of transonic buffet suppression by trailing edge flap. *Comput. Fluids* **2016**, *132*, 32–45. [[CrossRef](#)]
- Titchener, N.; Babinsky, H. Shock wave/boundary-layer interaction control using a combination of vortex generators and bleed. *AIAA J.* **2013**, *51*, 1221–1233. [[CrossRef](#)]
- Kouchi, T.; Yamaguchi, S.; Koike, S.; Nakajima, T.; Sato, M.; Kanda, H.; Yanase, S. Wavelet analysis of transonic buffet on a two-dimensional airfoil with vortex generators. *Exp. Fluids* **2016**, *57*, 166. [[CrossRef](#)]
- Jones, N.R.; Jarrett, J.P. Designing a shock control bump array for a transonic wing-body model. *AIAA J.* **2018**, *56*, 4801–4814. [[CrossRef](#)]
- Tian, Y.; Gao, S.; Liu, P.; Wang, J. Transonic buffet control research with two types of shock control bump based on RAE2822 airfoil. *Chin. J. Aeronaut.* **2017**, *30*, 1681–1696. [[CrossRef](#)]
- Smith, A.; Babinsky, H.; Fulker, J.; Ashill, P. Shock wave/boundary-layer interaction control using streamwise slots in transonic flows. *J. Aircr.* **2004**, *41*, 540–546. [[CrossRef](#)]
- Polivanov, P.A.; Sidorenko, A.A.; Maslov, A.A. Effective plasma buffet and drag control for laminar transonic aerofoil. *Proc. Inst. Mech. Eng. Part G* **2020**, *234*, 58–67. [[CrossRef](#)]
- Sidorenko, A.; Budovsky, A.; Polivanov, P.; Vishnyakov, O.; Sudakov, V.; Ishchenko, V. Suppression of transonic buffet with plasma vortex generators. *Thermophys. Aeromechanics* **2019**, *26*, 465–480. [[CrossRef](#)]
- Caruana, D.; Mignosi, A.; Corrège, M.; Le Pourhiet, A.; Rodde, A. Buffet and buffeting control in transonic flow. *Aerosp. Sci. Technol.* **2005**, *9*, 605–616. [[CrossRef](#)]
- Ren, K.; Chen, Y.; Gao, C.; Zhang, W. Adaptive control of transonic buffet flows over an airfoil. *Phys. Fluids* **2020**, *32*, 096106. [[CrossRef](#)]
- Li, D.; Zhao, S.; Da Ronch, A.; Xiang, J.; Drofelnik, J.; Li, Y.; Zhang, L.; Wu, Y.; Kintscher, M.; Monner, H.P. A review of modelling and analysis of morphing wings. *Prog. Aerosp. Sci.* **2018**, *100*, 46–62. [[CrossRef](#)]
- Nir, A.; Abramovich, H. Design, analysis and testing of a smart fin. *Compos. Struct.* **2010**, *92*, 863–872. [[CrossRef](#)]

15. Sinn, T.; Barrett, R. Design, manufacturing and test of a high lift secondary flight control surface with shape memory alloy post-buckled precompressed actuators. *Actuators* **2015**, *4*, 156–171. [[CrossRef](#)]
16. Sun, J.; Guan, Q.; Liu, Y.; Leng, J. Morphing aircraft based on smart materials and structures: A state-of-the-art review. *J. Intell. Mater. Syst. Struct.* **2016**, *27*, 2289–2312. [[CrossRef](#)]
17. Fincham, J.; Friswell, M. Aerodynamic optimisation of a camber morphing aerofoil. *Aerosp. Sci. Technol.* **2015**, *43*, 245–255. [[CrossRef](#)]
18. Wang, I.; Gibbs, S.C.; Dowell, E.H. Aeroelastic model of multisegmented folding wings: Theory and experiment. *J. Aircr.* **2012**, *49*, 911–921. [[CrossRef](#)]
19. Zhao, S.; Li, D.; Zhou, J.; Sha, E. Numerical and experimental study of a flexible trailing edge driving by pneumatic muscle actuators. *Actuators* **2021**, *10*, 142. [[CrossRef](#)]
20. Cooper, J.; Chekkal, I.; Cheung, R.; Wales, C.; Allen, N.; Lawson, S.; Peace, A.; Cook, R.; Standen, P.; Hancock, S. Design of a morphing wingtip. *J. Aircr.* **2015**, *52*, 1394–1403. [[CrossRef](#)]
21. Woods, B.K.; Bilgen, O.; Friswell, M.I. Wind tunnel testing of the fish bone active camber morphing concept. *J. Intell. Mater. Syst. Struct.* **2014**, *25*, 772–785. [[CrossRef](#)]
22. Thill, C.; Etches, J.; Bond, I.; Potter, K.; Weaver, P. Morphing skins. *Aeronaut. J.* **2008**, *112*, 117–139. [[CrossRef](#)]
23. Bilgen, O.; Kochersberger, K.B.; Inman, D.J.; Ohanian, O.J., III. Novel, bidirectional, variable-camber airfoil via macro-fiber composite actuators. *J. Aircr.* **2010**, *47*, 303–314. [[CrossRef](#)]
24. Li, D.; Liu, Q.; Wu, Y.; Xiang, J. Design and analysis of a morphing drag rudder on the aerodynamics, structural deformation, and the required actuating moment. *J. Intell. Mater. Syst. Struct.* **2018**, *29*, 1038–1049. [[CrossRef](#)]
25. Grigorie, T.; Botez, R.; Popov, A. How the airfoil shape of a morphing wing is actuated and controlled in a smart way. *J. Aerosp. Eng.* **2015**, *28*, 04014043. [[CrossRef](#)]
26. Lv, B.; Wang, Y.; Lei, P. Effects of trailing edge deflections driven by shape memory alloy actuators on the transonic aerodynamic characteristics of a super critical airfoil. *Actuators* **2021**, *10*, 160. [[CrossRef](#)]
27. Dimino, I.; Gallorini, F.; Palmieri, M.; Pispola, G. Electromechanical actuation for morphing winglets. *Actuators* **2019**, *8*, 42. [[CrossRef](#)]
28. Munday, D.; Jacob, J. Active control of separation on a wing with conformal camber. In Proceedings of the 39th Aerospace Sciences Meeting and Exhibit, Reno, NV, USA, 8–11 January 2001; p. 293.
29. Baldelli, D.H.; Lee, D.-H.; Peña, R.S.S.; Cannon, B. Modeling and control of an aeroelastic morphing vehicle. *J. Guid. Control Dyn.* **2008**, *31*, 1687–1699. [[CrossRef](#)]
30. Perera, M.; Guo, S. Optimal design of an aeroelastic wing structure with seamless control surfaces. *Proc. Inst. Mech. Eng. Part G* **2009**, *223*, 1141–1151. [[CrossRef](#)]
31. Ai, Q.; Azarpeyvand, M.; Lachenal, X.; Weaver, P.M. Aerodynamic and aeroacoustic performance of airfoils with morphing structures. *Wind Energy* **2016**, *19*, 1325–1339. [[CrossRef](#)]
32. Zhao, C.; Zhou, L.; Qiu, T. Research on flexible skin technique for adaptive bump inlet structure. *Aircr. Eng. Aerosp. Technol.* **2022**, *94*, 981–993. [[CrossRef](#)]
33. Lee, C.Y.; Kim, J.H. Active flutter suppression of smart-skin antenna structures with piezoelectric sensors and actuators. *Aerospace* **2021**, *8*, 257. [[CrossRef](#)]
34. Tsushima, N.; Su, W. Flutter suppression for highly flexible wings using passive and active piezoelectric effects. *Aerosp. Sci. Technol.* **2017**, *65*, 78–89. [[CrossRef](#)]
35. Wang, G.; Mian, H.H.; Ye, Z.-Y.; Lee, J.-D. Improved point selection method for hybrid-unstructured mesh deformation using radial basis functions. *AIAA J.* **2015**, *53*, 1016–1025. [[CrossRef](#)]
36. Cook, P.; Firmin, M.; McDonald, M. *Aerofoil RAE 2822: Pressure Distributions, and Boundary Layer and Wake Measurements*; AGARD Advisory Report; Advisory Group for Aerospace Research and Development: Neuilly sur Seine, France, 1979; p. A6.
37. Hou, Z.S.; Wang, Z. From model-based control to data-driven control: Survey, classification and perspective. *Inf. Sci.* **2013**, *235*, 3–35. [[CrossRef](#)]